J-Aggregates of *meso*- [2.2] Paracyclophanyl-BODIPY Dye for NIR-II Imaging

Zhipeng Liu (iamzpliu@njtech.edu.cn)
Nanjing Forestry University https://orcid.org/0000-0002-5458-9362
Kang Li
Nanjing Forestry University
Xingchen Duan
Nankai University
Zhiyong Jiang
Nanjing Forestry University
Dan Ding
Nankai University
Guo-qiang Zhang
Nankai University
Yuncong Chen
Nanjing University https://orcid.org/0000-0002-8406-4866

Article

Keywords: J-aggregation, NIR-II imaging

Posted Date: December 28th, 2020

DOI: https://doi.org/10.21203/rs.3.rs-122847/v1

Version of Record: A version of this preprint was published at Nature Communications on April 22nd, 2021. See the published version at https://doi.org/10.1038/s41467-021-22686-z.

Abstract

J-aggregation has been proved to be an efficient strategy for the development of fluorescent imaging agents in the second near-infrared (NIR-II, 1000–1700 nm) window. However, the design of NIR-II fluorescent J-aggregates is challenging due to the lack of suitable J-aggregation dyes. Herein, we report *meso*-[2.2]paracyclophanyl-3,5-bis-*N*,*N*-dimethylaminostyrl BODIPY (PCP-BDP2) as the first example of BODIPY dye with J-aggregation induced NIR-II fluorescence. PCP-BDP2 shows emission maximum at 795 nm in diluted solution and NIR-II emission at 1010 nm in the J-aggregation state. Mechanism studies reveal that the steric and conjugation effect of the PCP group on the BODIPY core plays key roles in the J-aggregation behavior and NIR-II fluorescence tuning. Notably, NIR-II emissive J-aggregates of PCP-BDP2 can be efficiently stabilized in the assembled nanoparticle. Taking advantage of high quantum yield and good photo-/chemo-stability, J-aggregates of PCP-BDP2 show high-resolution and long-term in vivo NIR-II imaging ability. Furthermore, J-aggregates of PCP-BDP2 can be utilized for lymph node imaging and fluorescence-guided surgery in the nude mouse, which demonstrates their potential clinical application. This study not only demonstrates BODIPY dye as a new J-aggregation platform for developing NIR-II imaging agents but also encourages further exploration on J-aggregation induced NIR-II emission of the other conventional organic dyes.

Introduction

Organic fluorescent dyes with emission wavelength in the second near-infrared (NIR-II, 1000–1700 nm) window have great promise for optical imaging because of their good biological compatibility, deep tissue penetration, high imaging resolution, and low auto-fluorescence.[1–4] Attempts to achieve NIR-II emission in organic dyes have focused mainly on molecular engineering strategy by creating large π−conjugate structure and installing strong electron-donating (D) and electron-accepting (A) groups. However, NIR-II emitting dyes are difficult to attain due to the lack of suitable π−conjugate scaffolds.[4, 5] To date, NIR-II dyes are mainly derived from the polymethine skeleton[6 – 11] and benzobisthiadiazole (BBTD) core,[2, 12–18] and rare examples are developed based on BODIPY,[19–22] squaraine,[23] as well as rhodamine.[24] In this context, exploring an alternative avenue to access NIR-II dyes is highly required.

A complementary approach is to create NIR-II fluorescent J-aggregates. J-aggregates, in which the transition dipole moments of individual molecules are in slip-stacked alignment, usually display different photophysical properties from those of monomers including red-shifted absorption and fluorescence spectra and enhanced quantum yields.[25–27] Benefiting from these unique characteristics of J-aggregates, J-aggregation is becoming a facile way to achieve NIR-II fluorescence. Elegant examples of NIR-II emissive J-aggregates of cyanine and squaraine dyes were given by Sletten,[28] Zhang,[29], and Fan[23] groups. However, advances in the J-aggregates with NIR-II emission are rather slow in comparison with fluorophores developed based on molecular engineering strategy due to the lack of diversified J-aggregate fluorescent dyes. J-aggregation requires molecules to pack in a slipped arrangement, however, fluorescent dyes with large π−conjugated structure tend to stack in a face-to-face packing mode (H-

aggregation).[30] As a result, rare fluorescent dyes show J-aggregation behavior except for cyanine, perylenediimide, chlorophylls and squaranines. [23, 27–29, 31–35]

BODIPY (4,4-difluoro-4-bora-3a,4a-diazas-indacene) dyes are well-known fluorescent dyes with excellent photophysical properties that enable them to be good candidates for biological sensing and imaging.[36, 37] Notably, recent studies revealed that BODIPY dyes are potential to be employed as novel J-aggregation scaffolds. Many BODIPY dyes have been reported to be J-aggregate in lipid vesicles,[38–43] aqueous solution[44–48], and crystalline state.[49–51] Moreover, several examples of BODIPY J-aggregates have been used for biological sensing and imaging. For example, Kim and co-workers developed a J-aggregating probe based on *meso*-ester-substituted BODIPY for tracking Eosinophil peroxidase activity in cancer cells.[46] Zheng and co-workers prepared aza-BODIPY J-aggregate-containing liposomal nanoparticles, which could be used for NIR-I cancer imaging.[42] Li and co-workers reported nano-assemblies of J-aggregated BODIPY as a stimuli-responsive tool for imaging oxidative stress in living systems.[43] Although numbers of fluorescent BODIPY J-aggregates have been reported, understanding the relationship between the structure and J-aggregation, as well as overcoming the aggregation-caused emission (ACQ) quenching are still required. Furthermore, exploring new building blocks for NIR-II emissive BODIPY J-aggregates remains a great challenge. In the course of our continuous efforts in the development of solid-state and NIR-II emissive BODIPY dyes,[21, 52, 53] we envisioned that J-aggregation of BODIPY dyes could be an efficient strategy to achieve NIR-II emission. Herein, we report a BODIPY dye (PCP-BDP2) that readily J-aggregates in aqueous solution by introducing [2, 2]paracyclophane (PCP) group to the *meso*-position of BODIPY (Fig. 1). PCP-BDP2 J-aggregates show both NIR (J_1-band, 900 nm) and NIR-II (J_2-band, 1010 nm) emission in aggregation state, and only NIR-II emission in crystalline powder state. By co-precipitation PCP-BDP2 with Pluronic F-127, the J-aggregates are stabilized in the assembled nanoparticle and show bright NIR-II emission with high fluorescence quantum yield (Φ_f) of 6.4%. We also demonstrated the promising NIR-II imaging ability of the J-aggregates both in vitro and in vivo, as well as the potential application in the clinic for fluorescence-guided surgery (FGS) in nude mice.

Results And Discussion

Design and synthesis. Due to the large π−conjugated frameworks, BODIPY dyes tend to aggregate in a face-to-face stacking mode (H-aggregation), and J-aggregation is usually not favored. As a result, most BODIPY dyes usually display ACQ in the aggregation state. To dismiss the strongly π−π interactions between the indacene plane and subsequently achieve the goal of J-aggregation, we introduced a PCP group with a three-dimension (3D) structure, to the *meso* position of BODIPY core. Moreover, we conjugated the strong electron-donating group, *N*,*N*-dimethylaminostyrl, to the 3,5- position of the PCP-BODIPY structure to realize the NIR-I emission (Fig. 1). Take advantage of red-shifted emission, J-aggregates of PCP-BOIDPY dye are expected to be fluorescent in the NIR-II region. The synthesis of PCP-BDP1 and PCP-BDP2 is outlined in Scheme S1. Additionally, two BODIPY dyes, Ph-BDP1[51] and Ph-

BDP2,[54] which have the phenyl group on the *meso*-position of BODIPY core, were synthesized for comparison.

X-ray single crystal structure analysis. To confirm the molecular design concept, we first investigated the molecular packing mode of PCP-BDP1 and PCP-BDP2 *via* single crystal structure analysis (Table S1). In the single crystal structure, the indacene planes of PCP-BDP1 and PCP-BDP2 are slightly bent due to the weak intermolecular interactions (Fig. 2 and S1). The PCP group is highly twisted to the BODIPY core. The dihedral angles between the phenyl ring that was attached to the BODIPY core and the indacene plane are ranging from 55.5^{o} to 58.5^{o}. In the molecular packing structure of PCP-BDP1, PCP groups are connected to the indacene plane through C-H···π (~ 3.8 Å) interactions. Due to the steric effect of the PCP group, the face-to-face molecular packing mode between the indacene plane is disfavored, as a result, PCP-BDP1 molecules are J-aggregated with a slipping angle of 38^{o}.[27] The distances between the borondipyrrole plane are ~ 3.7 Å. Ph-BDP1 show different molecular packing mode comparing to PCP-BDP1.[51] As shown in Figure S2, Ph-BDP1 molecules are arranged in a zigzag pattern through weak C-H···π interactions and no J-dimers were observed in the molecular packing structure. This difference demonstrates that the PCP group plays a key role in tuning the J-aggregation of BODIPY core. In PCP-BDP2, π···π interactions between the *N*,*N*-dimethylaminphenyl group and the indacene plane, the C-H···F hydrogen bond (~ 3.4 Å) between the PCP group and the borondipyrrole plane, and C-H···π (~ 3.8 Å) interactions between the PCP group and the *N*,*N*-dimethylaminphenyl group dominate the molecular packing structure of PCP-BDP2, which facilitate the J-aggregation packing mode. The slipping angle and the distance between each molecule are determined to be 36^{o} and ~ 3.3 Å, respectively (Fig. 2c).

Photophysical properties. Before investigating the photophysical properties of J-aggregates, firstly, we measured the absorption and emission spectra of PCP-BDP1 and PCP-BDP2 in diluted solutions. In dichloromethane (DCM), PCP-BDP1 displayed the main absorption band (λ_{abs}) centered at 523 nm (ε = 41900 $M^{-1}cm^{-1}$), and two emission bands centered at 524 nm and 554 nm, respectively (Figure S3). The sharp and narrow emission band at 524 nm can be assigned as the typical local excite (LE) emission of the BODIPY core, while the broad and weak emission band at 554 nm should be ascribed to the charge transfer (CT) emission band. In most cases, the phenyl ring at the *meso*-position has a very weak conjugation effect on the BODIPY core because of its free rotation.[55] For example, Ph-BDP1 only shows the LE emission at 515 nm in DCM, and the CT band around 550 nm is hardly to be distinguished from the LE emission. However, the free rotation of the PCP group in PCP-BDP1 is inhibited due to the steric effect of the PCP group, leading to the CT from the PCP group to the BODIPY core. This speculation was preliminary proved by measuring the viscosity-dependent emission spectra. As shown in Figure S4, the emission intensity at 554 nm is gradually increased with the viscosity-increasing from 0.6 to 630 cp, while the intensity at 524 nm is almost unchanged. This result suggests that the CT process was greatly enhanced due to the inhibited rotation of the PCP group in the high viscosity media. Moreover, PCP-BDP2 showed the absorption and emission bands centered at 722 nm and 795 nm, respectively, which is red-shifted in comparison with that of Ph-BDP2 (λ_{abs} = 700 nm and λ_{em} = 750 nm in DCM, Fig. 2d). This result

suggests that the CT process is more strengthened in PCP-BDP2 than in Ph-BDP2, which also confirms the electron-conjugating effect of the PCP group on the BODIPY core.

We further carried out the theoretical calculation to understand the different absorption and emission properties between these PCP and phenyl groups substituted BODIPY dyes (Table S2). Time-dependent density functional theory (TDDFT) results show that the main absorption and emission bands of Ph-BDP1 are contributed mainly by the transition from the highest occupied molecular orbital (HOMO) to the lowest unoccupied molecular orbital (LUMO) (Fig. 2e and S5a). Moreover, the HOMO and LUMO are delocalized on the indacene plane, while the phenyl ring at the *meso*-position has negligible contribution to the electronic structure of Ph-BDP1 in both ground and excited states. Different from that, the PCP group in PCP-BDP1 is conducive to the electron delocalization in both HOMO and LUMO (Fig. 2e and S5b). This difference makes the main absorption band of PCP-BDP1 is composed of both the first (S_1) and second (S_2) excited states, which mainly originated from the HOMO→LUMO, HOMO-1→LUMO and HOMO-3→LUMO transitions. The electronic transition of $S_1 \rightarrow S_0$ (ground state, f = 0.0900) can be ascribed to the CT emission, while the $S_2 \rightarrow S_0$ transition with relative large oscillator strength (f = 0.4344) is a fluorescent LE state. This result is consistent with the fluorescent spectrum of PCP-BDP1 obtained in DCM. The CT process from the PCP group to the indacene plane should be responsible for the different emission behavior of Ph-BDP1 and PCP-BDP1. Interestingly, the main absorption and emission bands of both Ph-BDP2 and PCP-BDP2 are contributed by the HOMO→LUMO transitions (Fig. 2e and S6). The HOMO and LUMO of Ph-BDP1 and the HOMO of PCP-BDP2 are delocalized on the whole molecular skeleton except for the phenyl and PCP groups. However, the LUMO of PCP-BDP2 is localized on the BODIPY core as well as the *meso*-phenyl ring of the PCP group. This feature favors the strengthened CT process, and therefore, the red-shifted absorption and emission bands of PCP-BDP2 in comparison with that of PCP-BDP1 can be rationalized.

Both the absorption and emission wavelength of PCP-BDP1 remain almost unchanged in different solvents, and only a slight increase of the absorbance and the emission intensity is observed in a polar solvent such as methanol and dimethylsulfoxide (DMSO) (Figure S7). All of these results demonstrate the weak CT of PCP-BDP1. Due to the donor (D)−π−acceptor (A) structure, PCP-BDP2 shows polarity dependent absorption and emission (Figure S8). The absorption and emission bands are red-shifted with the increased solvent polarity. For example, PCP-BDP2 exhibited λ_{em} in DMSO at 824 nm, which is 73 nm red-shifted relative to the λ_{em} of 751 nm in hexane. Interestingly, the emission intensity increment is also observed in solvents with relatively large viscosity, such as *o*-dichlorobenzene (1.32 cP at 25°C), 1,4-dioxane (1.20 cP at 25°C) and DMSO (1.98 cP at 25°C). This result suggests that the non-radiative decay process is inhibited due to the restricted intermolecular motion in these solvents with higher viscosity.

J-aggregation behavior in the aggregated state. To further explore the J-aggregation behavior of PCP-BDP1 and PCP-BDP2, we investigated their emission variation in the tetrahydrofuran (THF)-water binary solvents. In THF, PCP-BDP1 and PCP-BDP2 show one sharp absorption band at 523 and 718 nm, respectively. After the addition of water to the solution, the absorbance decreases and red-shifted to 532

and 748 nm when the water volumetric factions (f_w) increased to 99%, which indicates the formation of J-aggregates (Figure S9). In the emission spectra, the emission intensity at 520 nm and 560 nm of PCP-BDP1 remain unchanged with f_w increasing from 0 to 70%. With f_w of 80%, the emission intensity at 520 nm was distinctly increased, accompanied by the slightly red-shifted CT band. This result suggests that PCP-BDP1 begins to aggregate, the restricted molecular motion and enhanced CT process should be responsible for the enhanced LE emission and the red-shifted CT emission. Notably, when f_w reaches 90%, the LE emission is distinctly decreased, and the CT emission is almost disappeared. A new broad emission band ranging from 560 nm to 850 nm, which should be assigned as the emission of J-aggregates, is appeared simultaneously (Fig. 3a). Since the emission wavelength of J-aggregates is highly dependent on the size of the aggregates, the coexistence of the J-aggregates with different sizes is the reason for the formation of the broad emission band.[56]

PCP-BDP2 showed the same aggregation trend as PCP-BDP1. As shown in Fig. 3b, the emission intensity at 790 nm was enhanced and red-shifted to 820 nm with f_w increasing from 10–60%. The intramolecular motion restriction and the CT process enhancement induced by the viscosity and polarity increment should be responsible for the enhanced and red-shifted emission, respectively. With f_w of 70%, the emission at 820 nm was distinctly quenched, accompanied by the appearance of a new broad peak around 930 nm, suggesting the formation of J-aggregates. When f_w reaches 80% and 90%, most of the PCP-BDP2 molecules may be aggregated to J-aggregate, as a result, the emission around 800 nm is almost disappeared, while the emission band of J-aggregates at approximately 900 nm (J_1-band) is enhanced. Notably, a weak NIR-II emission band around 1000 nm (J_2-band) was also observed as the side peak of the main emission band, which suggests that the emission of PCP-BDP2 J-aggregates is capable of red-shifted to the NIR-II region when the more condensed J-aggregates are formed.

To verify this speculation, we further measured the emission spectra of PCP-BDP1 and PCP-BDP2 in the solid state. The crystalline powder of PCP-BDP1 showed multiple J-aggregates emission bands at 570 nm, 640 nm, and 685 nm, respectively, which is contributed by J-aggregates with different energies (Fig. 3c). Notably, PCP-BDP2 displayed one broad J-aggregates emission centered at 1010 nm, which is consistent with the J_2-band observed in THF-water binary solvent with f_w of 99% (Fig. 3d). This result confirms that the condensed molecular packing mode should be responsible for the generation of the J_2-band of PCP-BDP2. Additionally, we also measured the emission behavior of Ph-BDP1 and Ph-BDP2 in THF-water. With the f_w increasing from 0 to 90%, the emission of both two compounds was gradually decreased, indicating the typical ACQ behavior (Figure S10). These results further demonstrated that the PCP group plays a key role in the J-aggregation behavior of PCP-BDP1 and PCP-BDP2.

Encouraged by the NIR-II emission capability of PCP-BDP2 J-aggregates observed in both THF-water and solid-state, we investigated that whether the NIR-II emissive J-aggregates could be stabilized in nanoparticles (NPs) and be employed for the NIR-II imaging. we prepared PCP-BDP2 NPs by encapsulating the PCP-BDP2 aggregates into a Pluronic F-127 matrix. The PCP-BDP2 NPs showed a spherical morphology with a diameter of ~ 70 nm, which was characterized using transmission electron

microscopy (TEM) (Fig. 3e). The average diameter of PCP-BDP2 NPs was measured to be ~ 75 nm by a dynamic light scattering (DLS) experiment with a low polydispersity index (PDI) of 0.081 (Fig. 3f). In PBS buffer, the PCP-BDP2 NPs showed λ_{abs} and λ_{em} around 750 and 1010 nm, respectively, which is comparable with those observed in the aggregation state. This result suggests that the J-aggregates can be efficiently stabilized in the Pluronic F-127 matrix.

The PCP-BDP2 NPs showed relatively high Φ_f in PBS buffer. The calculated Φ_f value for PCP-BDP2 NPs was 6.4% (reference dye IR 26, Φ_f = 0.1%), which is higher than most reported NIR-II emissive BODIPY dyes and J-aggregates such as NJ1060 (1%),[21] and NIR-II-WAZABY-01 (0.8%).[20] Furthermore, after continuous laser irradiation (808 nm, 100 mW/cm^2) for 60 min, the NIR-II emission intensities of PCP-BDP2 NPs remained almost unchanged, however, another famous NIR-II fluorophore, IR1061, showed rapidly decayed emission from 100–75% under the same conditions (Fig. 3h). Moreover, PCP-BDP2 NPs showed no apparent absorption and emission spectral change in PBS in the presence of glutathione, cysteine, and hydrogen peroxide (Figure S11). These results demonstrate the good photo- and chemical-stability of PCP-BDP2 NPs.

In vitro imaging. To verify the biological imaging capability of PCP-BDP2 NPs, we carried out both the in vitro and in vivo NIR-II fluorescence imaging experiments. An 808 laser was used as the excitation resource because of its general availability and reduced biological absorption. A clinically approved NIR-I dye, ICG, was employed as a control. The PL intensity of PCP-BDP2 NPs with different concentrations was detected, and the NIR-II emission signals of PCP-BDP2 NPs showed a linear increase with the concentration, which is consistent with the above results that NIR-II emissive J-aggregates is highly related to the degree of aggregation (Fig. 4a and 4b). Besides, the NIR-II fluorescence signals of PCP-BDP2 NPs and ICG under the different thickness of chicken tissues were collected, the NPs showed good NIR-II imaging penetration depth up to 8 mm, which is higher than the 6 mm of ICG (Fig. 4c). Altogether, these results indicated that PCP-BDP2 NPs hold the promise to be a superb NIR-II fluorescent dye than ICG.

In vivo imaging. We further carried out in vivo NIR-II imaging of cerebral vasculature and hindlimb with the PCP-BDP2 NPs. The NPs in PBS were injected into mice via the tail vein. After the injection for 5 min, the blood vessels in both the brain and hindlimb can be visualized from the surrounding background tissue with high resolution. The brightness and clarity of PCP-BDP2 NPs were higher than that of ICG with the same imaging conditions, implying that the PCP-BDP2 NPs can offer better imaging quality than ICG (Fig. 4d and 4f), which was quantitatively analyzed and compared (Fig. 4e and 4 g). Moreover, the fluorescence signal of PCP-BDP2 NPs decreased gradually with the time increased from 5 min to 24 h, while the fluorescence of ICG is almost undetectable when the time increased to 8 h (Figure S12 and S13). Besides, the PCP-BDP2 NPs were found to accumulate in the liver and spleen, properly due to the uptake by mononuclear phagocytic system-related organs (Figure S14). All the above imaging results demonstrate the promising high-resolution and long-term NIR-II imaging ability of the PCP-BDP2 NPs.

Lymph node imaging. The lymphatic system is important for maintaining fluid homeostasis and immunity, which is increasingly considered as a conduit for the metastasis of a variety of cancers such as breast, melanoma and so on.[57] Optical imaging of the lymphatic system can map lymphatic drainage, locate sentinel lymph node (SLN), and visualize multiple lymph nodes.[58, 59] In this experiment, PCP-BDP2 NPs were used for in vivo imaging to assess its ability for mapping lymph nodes. The PCP-BDP2 NPs (50 μL,1 mg/mL) was subcutaneously injected into the footpads of nude mice, the lymphatic vasculature and the sentinel lymph node (SLN) was observed immediately (Fig. 5a), and it was still clear after 5 h injection (Fig. 5b). And then the SLN with a diameter of less than 1 mm was removed precisely with the guidance of the fluorescence signal of PCP-BDP2 NPs (Fig. 5c), and the (H&E) histological staining could prove again (Fig. 5d).

Image-guided surgery. Recently, NIR-II fluorescence-guided cancer surgery has been proven feasible clinically, which reduce cancer recurrence and promote the outcomes of cancer surgery.[4, 60] To demonstrate that the strong NIR-II fluorescence signal of PCP-BDP2 endow its ability for image-guided cancer surgery, the peritoneal carcinomatosis-bearing mouse model was established, which scatter numerous tumor nodules of various sizes in the peritoneal cavity, especially those with diameters < 1 mm. After the PCP-BDP2 NPs were intravenously injected into the mice for 24 h, the surgery was first performed by a surgeon by opening the mouse abdomen. As we selected luciferase-expressed 4T1 tumors that exhibited bioluminescence after injection with D-luciferin, so the signals of fluorescence of PCP-BDP2 NPs and the bioluminescence of luciferase were well colocalized (Fig. 6a). And then lots of large tumor nodules with diameters > 1 mm were removed by the surgeon's naked eyes. Then with the guidance of high brightness of PCP-BDP2 NPs, smaller tumor nodules were resected (Fig. 6c). The well-overlapped bioluminescence and fluorescence signals of the removed nodules indicate those were indeed tumors (Fig. 6b), which was also proved by the hematoxylin and eosin (H&E) staining (Fig. 6d), and these results together demonstrate the accuracy of operation.

Conclusion

In summary, we have demonstrated a BODIPY dye (PCP-BDP2) with J-aggregation induced emission in the NIR-II biological window by introducing a [2, 2]paracyclophane (PCP) group to the *meso*-position of 3,5-bis-*N*,*N*-dimethylaminostyrl BODIPY. Single crystal X-ray structure analysis and DFT calculation reveal the PCP group plays a key role in the photophysical property and J-aggregation tuning. Due to the conjugation effect of the PCP group, PCP-BDP2 shows λ_{em} approximately at 795 nm, which is larger red-shifted comparing to its analog Ph-BDP2 (λ_{em} = 750 nm) with phenyl ring substituted at *meso*-position. PCP-BDP2 is preferred to J-aggregate in the aggregation state. Notably, PCP-BDP2 J-aggregates show both NIR-I (J_1-band, 900 nm) and NIR-II (J_2-band, 1010 nm) emission in THF-water binary solvent, and only the NIR-II emission in crystalline powder state. The J-aggregate of PCP-BDP2 can be efficiently stabilized in the assembled nanoparticle, and show bright NIR-II emission with a high Φ_f of 6.4%. We also demonstrate the promising NIR-II imaging ability of the J-aggregates both in vitro and in vivo. PCP-BDP2 NPs show good photo-/chemo-stability and NIR-II imaging penetration, which facilitates its high-

resolution and long-term NIR-II imaging ability. Furthermore, we demonstrate the potential application in the clinic for lymph node imaging and fluorescence-guided surgery in nude mice. The results from this fundamental research provide insights for not only molecular engineering J-aggregation of BODIPY dyes for NIR-II imaging but also manipulating desired optical properties of luminescent dyes for potential applications in biological sensing and imaging.

Declarations

Conflicts of interest

There are no conflicts to declare.

Acknowledgments

This work was financially supported by the National Natural Science Foundation of China (2197115, 51873092 and 51961160730), the National Key R&D Program of China (Intergovernmental cooperation project, 2017YFE0132200), Tianjin Science Fund for Distinguished Young Scholars (19JCJQJC61200), the Science and Technology Project of Tianjin (20JCYBJC01140), the Fundamental Research Funds for the Central Universities, Nankai University.

Supplementary Information

accompanies this paper at http://www.nature.com/naturecommunications.

References

1. Welsher K, Liu Z, Sherlock SP, Robinson JT, Chen Z, Daranciang D*, et al.* A route to brightly fluorescent carbon nanotubes for near-infrared imaging in mice. *Nat. Nanotechnol.* **4**, 773-780 (2009).
2. Antaris AL, Chen H, Cheng K, Sun Y, Hong G, Qu C*, et al.* A small-molecule dye for NIR-II imaging. *Nat. Mater.* **15**, 235-242 (2016).
3. Li C, Chen G, Zhang Y, Wu F, Wang Q. Advanced fluorescence imaging technology in the near-infrared-II window for biomedical applications. *J. Am. Chem. Soc.* **142**, 14789-14804 (2020).
4. Zhu S, Tian R, Antaris AL, Chen X, Dai H. Near-infrared-II molecular dyes for cancer imaging and surgery. *Adv. Mater.* **31**, e1900321 (2019).
5. Li L, Dong X, Li J, Wei J. A short review on nir-ii organic small molecule dyes. *Dyes Pigm.* **183**, 108756 (2020).
6. Wang S, Fan Y, Li D, Sun C, Lei Z, Lu L*, et al.* Anti-quenching NIR-II molecular fluorophores for in vivo high-contrast imaging and ph sensing. *Nat Commun* **10**, 1058 (2019).
7. Li B, Lu L, Zhao M, Lei Z, Zhang F. An efficient 1064 nm NIR-II excitation fluorescent molecular dye for deep-tissue high-resolution dynamic bioimaging. *Angew. Chem. Int. Ed.* **57**, 7483-7487 (2018).

8. Prosposito P, Casalboni M, De Matteis F, Glasbeek M, Quatela A, van Veldhoven E*, et al.* Femtosecond dynamics of ir molecules in hybrid materials. *J. Lumin.* **94**, 641-644 (2001).
9. Cosco ED, Caram JR, Bruns OT, Franke D, Day RA, Farr EP*, et al.* Flavylium polymethine fluorophores for near- and shortwave infrared imaging. *Angew. Chem. Int. Ed.* **56**, 13126-13129 (2017).
10. Ding B, Xiao Y, Zhou H, Zhang X, Qu C, Xu F*, et al.* Polymethine thiopyrylium fluorophores with absorption beyond 1000 nm for biological imaging in the second near-infrared subwindow. *J. Med. Chem.* **62**, 2049-2059 (2019).
11. Lei Z, Sun C, Pei P, Wang S, Li D, Zhang X*, et al.* Stable, wavelength-tunable fluorescent dyes in the NIR-II region for in vivo high-contrast bioimaging and multiplexed biosensing. *Angew. Chem. Int. Ed.* **58**, 8166-8171 (2019).
12. Yang Q, Ma Z, Wang H, Zhou B, Zhu S, Zhong Y*, et al.* Rational design of molecular fluorophores for biological imaging in the NIR-II window. *Adv. Mater.* **29**, (2017).
13. Liu S, Chen C, Li Y, Zhang H, Liu J, Wang R*, et al.* Constitutional isomerization enables bright NIR-II aiegen for brain-inflammation imaging. *Adv. Funct. Mater.* **30**, 1908125 (2019).
14. Sun Y, Qu C, Chen H, He M, Tang C, Shou K*, et al.* Novel benzo-bis(1,2,5-thiadiazole) fluorophores for in vivo NIR-II imaging of cancer. *Chem. Sci.* **7**, 6203-6207 (2016).
15. Qian G, Dai B, Yu D, Zhan J, Zhang Z, Ma D*, et al.* Band gap tunable, donor–acceptor–donor charge-transfer heteroquinoid-based chromophores: Near infrared photoluminescence and electroluminescence. *Chem. Mater.* **20**, 6208–6216 (2008).
16. Mamada M, Shima H, Yoneda Y, Shimano T, Yamada N, Kakita K*, et al.* A unique solution-processable n-type semiconductor material design for high-performance organic field-effect transistors. *Chem. Mater.* **27**, 141-147 (2015).
17. Fang Y, Shang J, Liu D, Shi W, Li X, Ma H. Design, synthesis, and application of a small molecular NIR-II fluorophore with maximal emission beyond 1200 nm. *J. Am. Chem. Soc.* **142**, 15271-15275 (2020).
18. Wan H, Yue J, Zhu S, Uno T, Zhang X, Yang Q*, et al.* A bright organic NIR-II nanofluorophore for three-dimensional imaging into biological tissues. *Nat Commun* **9**, 1171 (2018).
19. Xu G, Yan Q, Lv X, Zhu Y, Xin K, Shi B*, et al.* Imaging of colorectal cancers using activatable nanoprobes with second near-infrared window emission. *Angew. Chem. Int. Ed.* **57**, 3626-3630 (2018).
20. Godard A, Kalot G, Pliquett J, Busser B, Le Guevel X, Wegner KD*, et al.* Water-soluble aza-bodipys: Biocompatible organic dyes for high contrast in vivo NIR-II imaging. *Bioconjug Chem* **31**, 1088-1092 (2020).
21. Bai L, Sun P, Liu Y, Zhang H, Hu W, Zhang W*, et al.* Novel aza-bodipy based small molecular NIR-II fluorophores for in vivo imaging. *Chem. Commun.* **55**, 10920-10923 (2019).
22. Strategic construction of ethene-bridged bodipy arrays with absorption bands reaching the near-infrared II region. *Org. Lett.* **22**, 7513-7517 (2020).

23. Sun P, Wu Q, Sun X, Miao H, Deng W, Zhang W*, et al.* J-aggregate squaraine nanoparticles with bright NIR-II fluorescence for imaging guided photothermal therapy. *Chem. Commun.* **54**, 13395-13398 (2018).
24. Rathnamalala CSL, Gayton JN, Dorris AL, Autry SA, Meador W, Hammer NI*, et al.* Donor-acceptor-donor NIR II emissive rhodindolizine dye synthesized by C-H bond functionalization. *J. Org. Chem.* **84**, 13186-13193 (2019).
25. Scheibe G. ber die veränderlichkeit der absorptionsspektren in lösungen und die nebenvalenzen als ihre ursache. *Angew. Chem.* **50**, 212-219 (1936).
26. Jelly EE. Spectral absorption and fluorescence of dyes in the molecular state. *Nature* **138**, 1009-1010 (1936).
27. Wurthner F, Kaiser TE, Saha-Moller CR. J-aggregates: From serendipitous discovery to supramolecular engineering of functional dye materials. *Angew. Chem. Int. Ed.* **50**, 3376-3410 (2011).
28. Chen W, Cheng CA, Cosco ED, Ramakrishnan S, Lingg JGP, Bruns OT*, et al.* Shortwave infrared imaging with J-aggregates stabilized in hollow mesoporous silica nanoparticles. *J. Am. Chem. Soc.* **141**, 12475-12480 (2019).
29. Sun C, Li B, Zhao M, Wang S, Lei Z, Lu L*, et al.* J-aggregates of cyanine dye for NIR-II in vivo dynamic vascular imaging beyond 1500 nm. *J. Am. Chem. Soc.* **141**, 19221-19225 (2019).
30. Chen Z, Lohr A, Saha-Moller CR, Wurthner F. Self-assembled pi-stacks of functional dyes in solution: Structural and thermodynamic features. *Chem. Soc. Rev.* **38**, 564-584 (2009).
31. Cao W, Sletten EM. Fluorescent cyanine dye J-aggregates in the fluorous phase. *J. Am. Chem. Soc.* **140**, 2727-2730 (2018).
32. Kaiser TE, Wang H, Stepanenko V, Wurthner F. Supramolecular construction of fluorescent J-aggregates based on hydrogen-bonded perylene dyes. *Angew. Chem. Int. Ed.* **46**, 5541-5544 (2007).
33. Yagai S, Seki T, Karatsu T, Kitamura A, Wurthner F. Transformation from H- to J-aggregated perylene bisimide dyes by complexation with cyanurates. *Angew. Chem. Int. Ed.* **47**, 3367-3371 (2008).
34. Kaiser TE, Stepanenko V, Wurthner F. Fluorescent j-aggregates of core-substituted perylene bisimides: Studies on structure-property relationship, nucleation-elongation mechanism, and sergeants-and-soldiers principle. *J. Am. Chem. Soc.* **131**, 6719-6732 (2009).
35. Cai K, Xie J, Zhang D, Shi W, Yan Q, Zhao D. Concurrent cooperative J-aggregates and anticooperative H-aggregates. *J. Am. Chem. Soc.* **140**, 5764-5773 (2018).
36. Kowada T, Maeda H, Kikuchi K. Bodipy-based probes for the fluorescence imaging of biomolecules in living cells. *Chem. Soc. Rev.* **44**, 4953-4972 (2015).
37. Zhang J, Wang N, Ji X, Tao Y, Wang J, Zhao W. Bodipy-based fluorescent probes for biothiols. *Chem. Eur. J.* **26**, 4172-4192 (2020).
38. Tleugabulova D, Zhang Z, Brennan JD. Characterization of bodipy dimers formed in a molecularly confined environment. *The Journal of Physical Chemistry B* **106**, 13133-13138 (2002).

39. Bergström F, Mikhalyov I, Hägglöf P, Wortmann R, Ny T, Johansson LBÅ. Dimers of dipyrromethene boron difluoride (bodipy) with light spectroscopic applications in chemistry and biology. *J. Am. Chem. Soc.* **124**, 196-204 (2002).
40. Yan Z, Wang M, Shi M, He Y, Zhang Y, Qiu S*, et al.* Amphiphilic bodipy dye aggregates in polymeric micelles for wavelength-dependent photo-induced cancer therapy. *J. Mater. Chem. B* **8**, 6886-6897 (2020).
41. Chen Z, Liu Y, Wagner W, Stepanenko V, Ren X, Ogi S*, et al.* Near-IR absorbing J-aggregate of an amphiphilic BF_2-azadipyrromethene dye by kinetic cooperative self-assembly. *Angew. Chem. Int. Ed.* **56**, 5729-5733 (2017).
42. Cheng MHY, Harmatys KM, Charron DM, Chen J, Zheng G. Stable J-aggregation of an aza-bodipy-lipid in a liposome for optical cancer imaging. *Angew. Chem. Int. Ed.* **58**, 13394-13399 (2019).
43. Su M, Li S, Zhang H, Zhang J, Chen H, Li C. Nano-assemblies from J-aggregated dyes: A stimuli-responsive tool applicable to living systems. *J. Am. Chem. Soc.* **141**, 402-413 (2019).
44. Choi S, Bouffard J, Kim Y. Aggregation-induced emission enhancement of a meso-trifluoromethyl bodipy via J-aggregation. *Chem. Sci.* **5**, 751-755 (2014).
45. Kim S, Bouffard J, Kim Y. Tailoring the solid-state fluorescence emission of bodipy dyes by meso substitution. *Chem. Eur. J.* **21**, 17459-17465 (2015).
46. Kim TI, Hwang B, Lee B, Bae J, Kim Y. Selective monitoring and imaging of eosinophil peroxidase activity with a J-aggregating probe. *J. Am. Chem. Soc.* **140**, 11771-11776 (2018).
47. Yang L, Fan G, Ren X, Zhao L, Wang J, Chen Z. Aqueous self-assembly of a charged bodipy amphiphile via nucleation-growth mechanism. *Phys. Chem. Chem. Phys.* **17**, 9167-9172 (2015).
48. Jiang L, Gao H, Gai LZ, Shen Z. J-aggregation induced emission enhancement of a thienyl substituted bis(difluoroboron)-1,2-bis((1H-pyrrol-2-yl)methylene)hydrazine (bophy) dye. *New J. Chem.* **42**, 8271-8275 (2018).
49. Vu TT, Badré S, Dumas-Verdes Cc, Vachon J-J, Julien C, Audebert P*, et al.* New hindered bodipy derivatives: Solution and amorphous state fluorescence properties. *J. Phys. Chem. C* **113**, 11844-11855 (2009).
50. Spies C, Huynh A-M, Huch V, Jung G. Correlation between crystal habit and luminescence properties of 4,4-difluoro-1,3-dimethyl-4-bora-3a,4a-diaza-s-indacene, an asymmetric bodipy dye. *J. Phys. Chem. C* **117**, 18163-18169 (2013).
51. Duan C, Zhou Y, Shan G-G, Chen Y, Zhao W, Yuan D*, et al.* Bright solid-state red-emissive bodipys: Facile synthesis and their high-contrast mechanochromic properties. *Journal of Materials Chemistry C* **7**, 3471-3478 (2019).
52. Wang X, Wu Y, Liu Q, Li Z, Yan H, Ji C*, et al.* Aggregation-induced emission (AIE) of pyridyl-enamido-based organoboron luminophores. *Chem. Commun.* **51**, 784-787 (2015).
53. Tian D, Qi F, Ma H, Wang X, Pan Y, Chen R*, et al.* Domino-like multi-emissions across red and near infrared from solid-state 2-/2,6-aryl substituted bodipy dyes. *Nat. Commun.* **9**, 2688 (2018).

54. Deniz E, Isbasar GC, Bozdemir OA, Yildirim LT, Siemiarczuk A, Akkaya EU. Bidirectional switching of near IR emitting boradiazaindacene fluorophores. *Org. Lett.* **10**, 3401-3403 (2008).
55. Lu H, Mack J, Yang Y, Shen Z. Structural modification strategies for the rational design of red/NIR region bodipys. *Chem. Soc. Rev.* **43**, 4778-4823 (2014).
56. Muenter AA, Brumbaugh DV, Apolito J, Horn LA, Spano FC, Mukamel S. Size dependence of excited-state dynamics for J-aggregates at silver bromide interfaces. *J. Phys. Chem.* **96**, 2783-2790 (1992).
57. Pereira ER, Kedrin D, Seano G, Gautier O, Meijer EFJ, Jones D*, et al.* Lymph node metastases can invade local blood vessels, exit the node, and colonize distant organs in mice. *Science* **359**, 1403-1407 (2018).
58. Tian R, Ma H, Zhu S, Lau J, Ma R, Liu Y*, et al.* Multiplexed NIR-II probes for lymph node-invaded cancer detection and imaging-guided surgery. *Adv. Mater.* **32**, e1907365 (2020).
59. Philp L, Chan H, Rouzbahman M, Overchuk M, Chen J, Zheng G*, et al.* Use of porphysomes to detect primary tumour, lymph node metastases, intra-abdominal metastases and as a tool for image-guided lymphadenectomy: Proof of concept in endometrial cancer. *Theranostics* **9**, 2727-2738 (2019).
60. Chen Y, Zhang H, Lei Z, Zhang F. Recent advances in intraoperative nerve bioimaging: Fluorescence-guided surgery for nerve preservation. *Small Structures* **1**, 2000036 (2020).

Figures

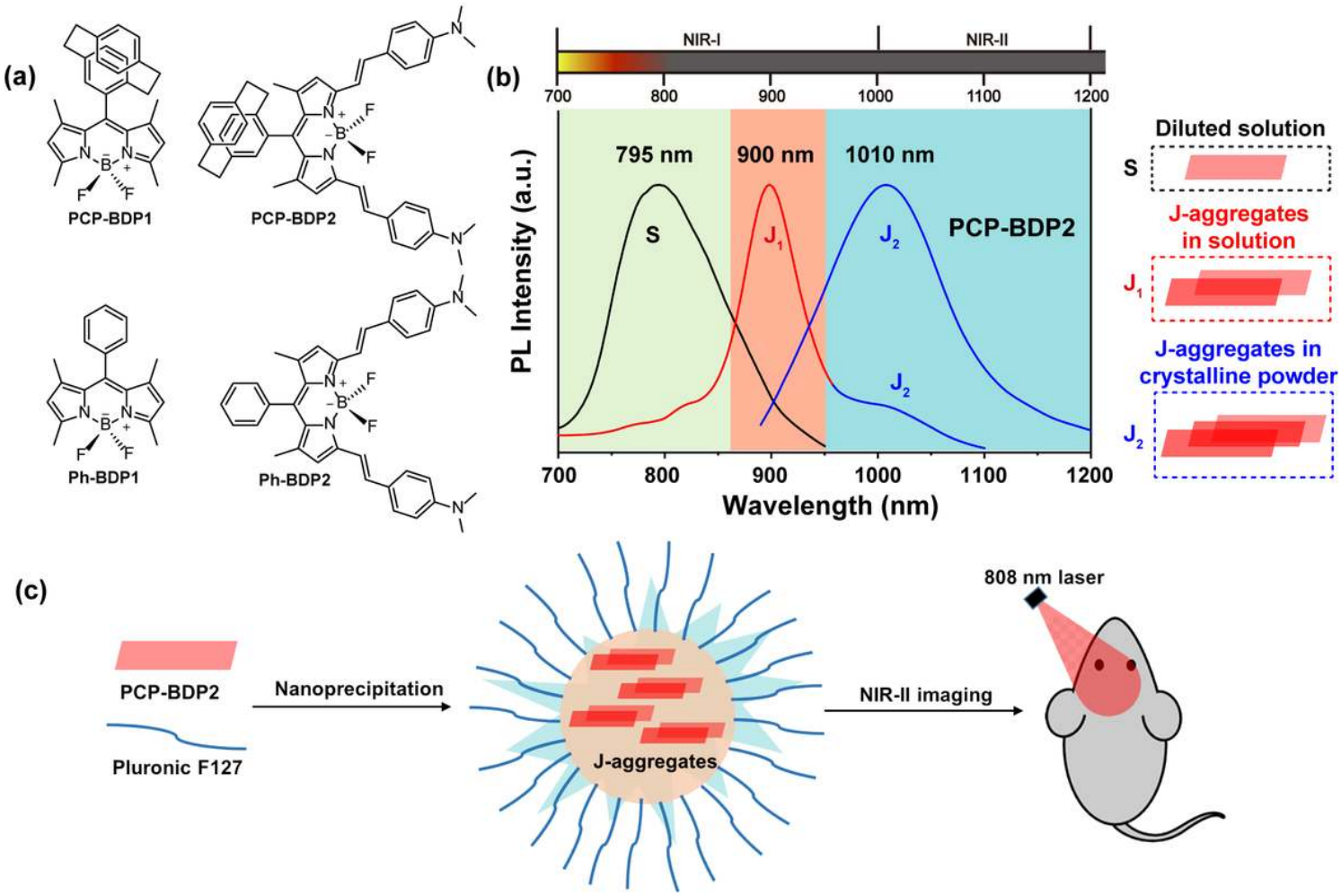

Figure 1

Molecular structures and working principle. (a) Chemical structures of PCP-BDP1, PCP-BDP2, Ph-BDP1, and Ph-BDP2. (b) Fluorescence spectra of PCP-BDP2 in diluted dichloromethane solution (10 mM) (black line), THF-water binary solvents (10 mM, 1: 9, v/v) (red line), and the crystalline powder (blue line). (c) Schematic illustration of the construction of the PCP-BDP2 nanoparticles for NIR-II imaging.

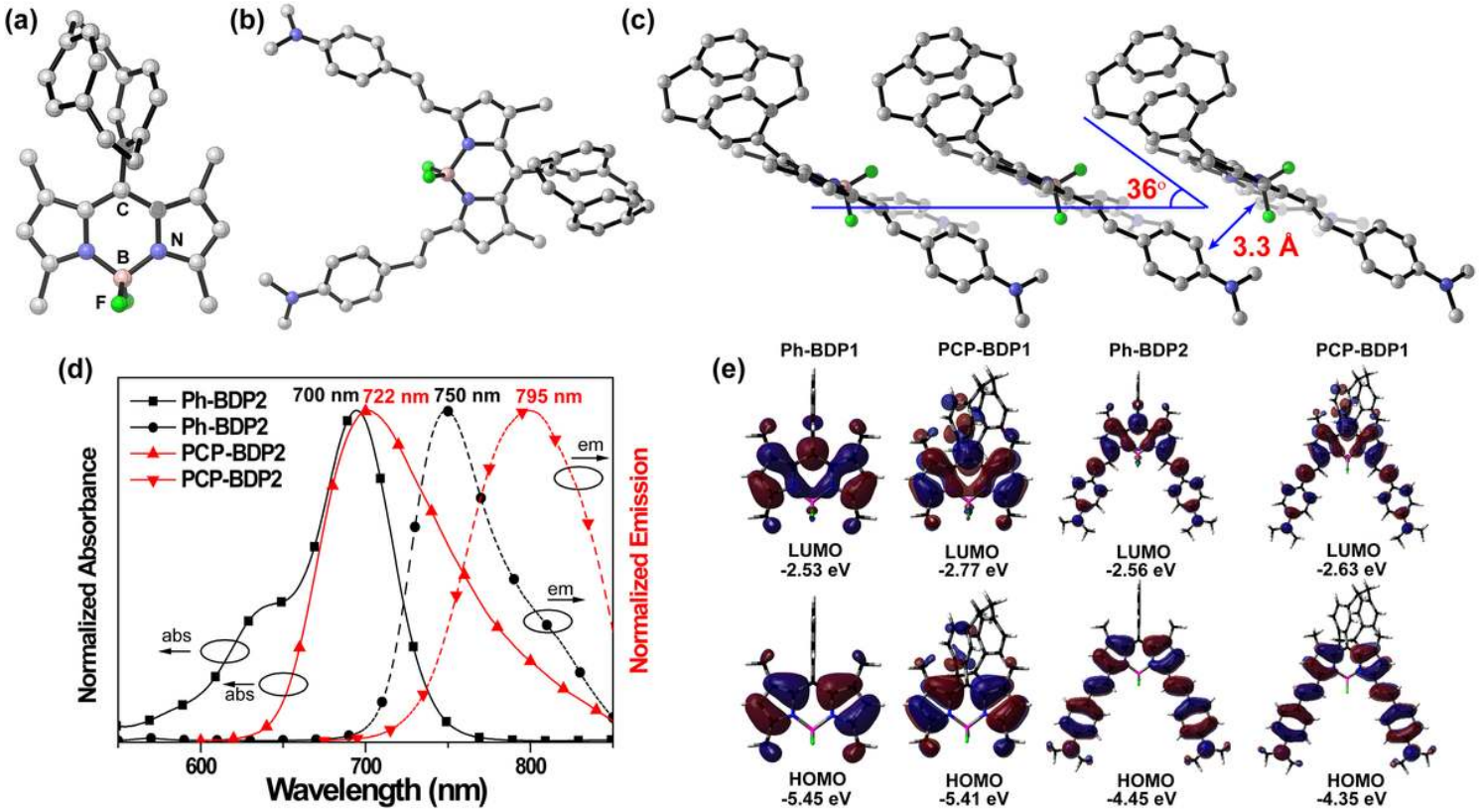

Figure 2

Crystal structures and photophysical properties. Ball and stick illustration of the X-ray structure of PCP-BDP1 (a, CCDC No. 2047734) and PCP-BDP2 (b, CCDC No. 2047734). (c) Molecular packing diagram of PCP-BDP2. Solvent molecules and H atoms are omitted for clarity. (d) Normalized absorption and emission spectra of Ph-BDP2 (black line) and PCP-BDP2 (red line) in DCM (10 μM). (e) Calculated frontier molecular orbitals for Ph-BDP1, PCP-BDP1, Ph-BDP2, and PCP-BDP2 and their orbital energies in the optimized excited state.

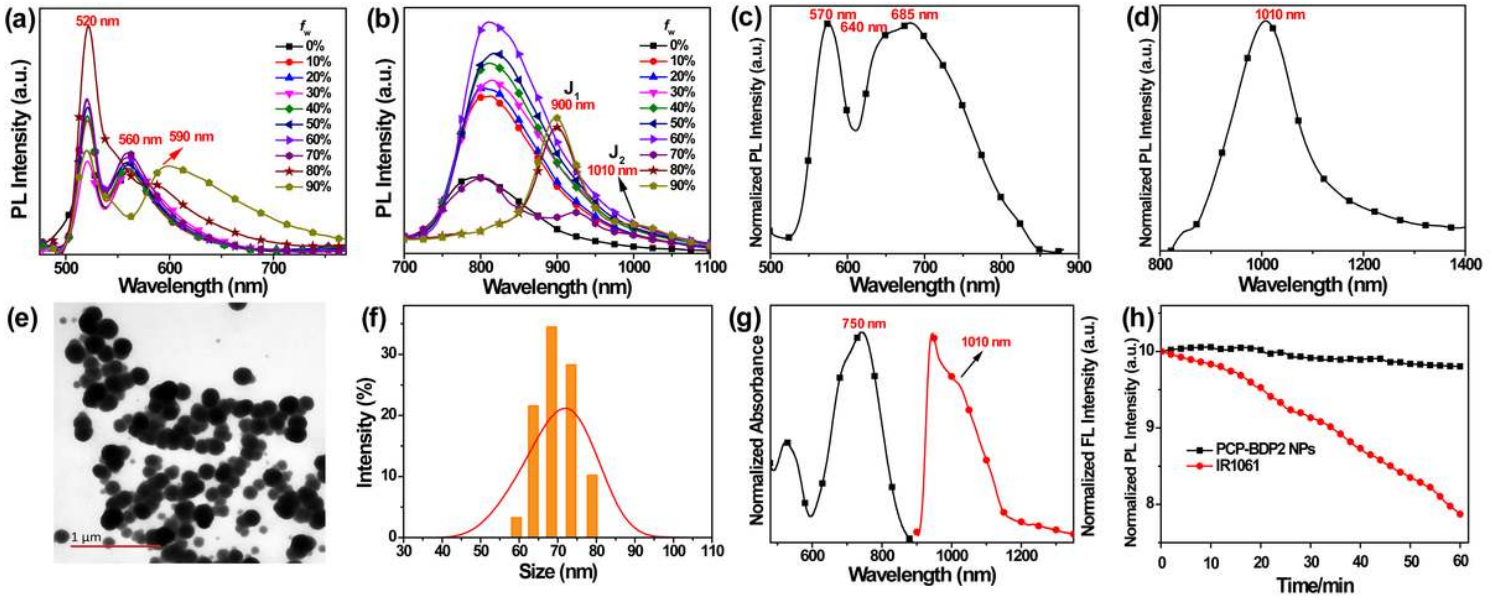

Figure 3

Crystal structures and photophysical properties. Ball and stick illustration of the X-ray structure of PCP-BDP1 (a, CCDC No. 2047734) and PCP-BDP2 (b, CCDC No. 2047734). (c) Molecular packing diagram of PCP-BDP2. Solvent molecules and H atoms are omitted for clarity. (d) Normalized absorption and emission spectra of Ph-BDP2 (black line) and PCP-BDP2 (red line) in DCM (10 μM). (e) Calculated frontier molecular orbitals for Ph-BDP1, PCP-BDP1, Ph-BDP2, and PCP-BDP2 and their orbital energies in the optimized excited state.

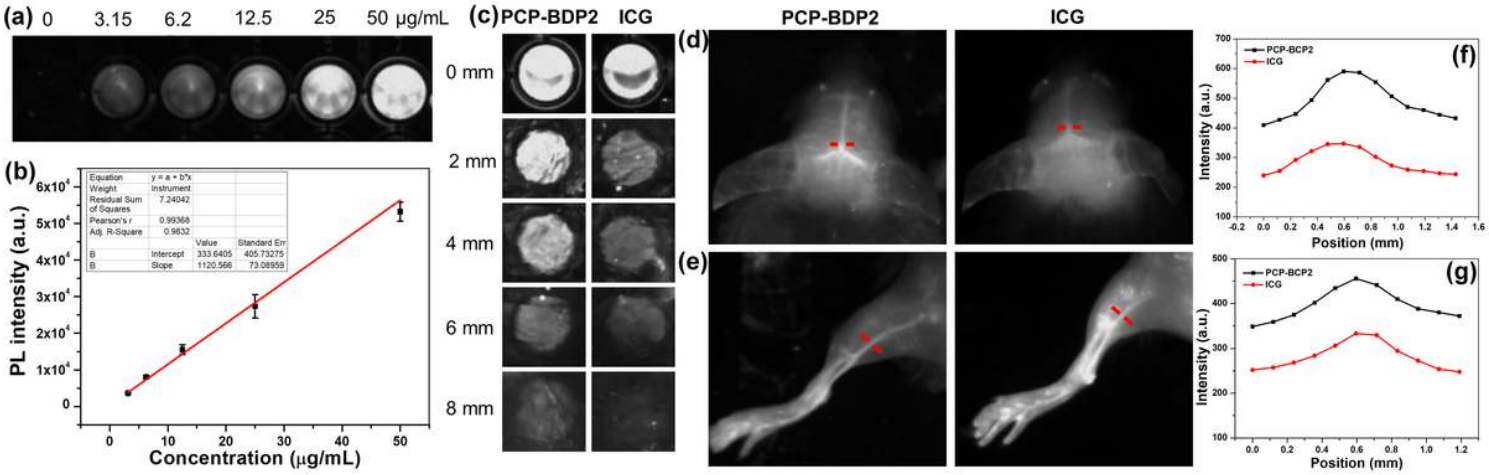

Figure 4

Crystal structures and photophysical properties. Ball and stick illustration of the X-ray structure of PCP-BDP1 (a, CCDC No. 2047734) and PCP-BDP2 (b, CCDC No. 2047734). (c) Molecular packing diagram of PCP-BDP2. Solvent molecules and H atoms are omitted for clarity. (d) Normalized absorption and emission spectra of Ph-BDP2 (black line) and PCP-BDP2 (red line) in DCM (10 μM). (e) Calculated frontier molecular orbitals for Ph-BDP1, PCP-BDP1, Ph-BDP2, and PCP-BDP2 and their orbital energies in the optimized excited state.

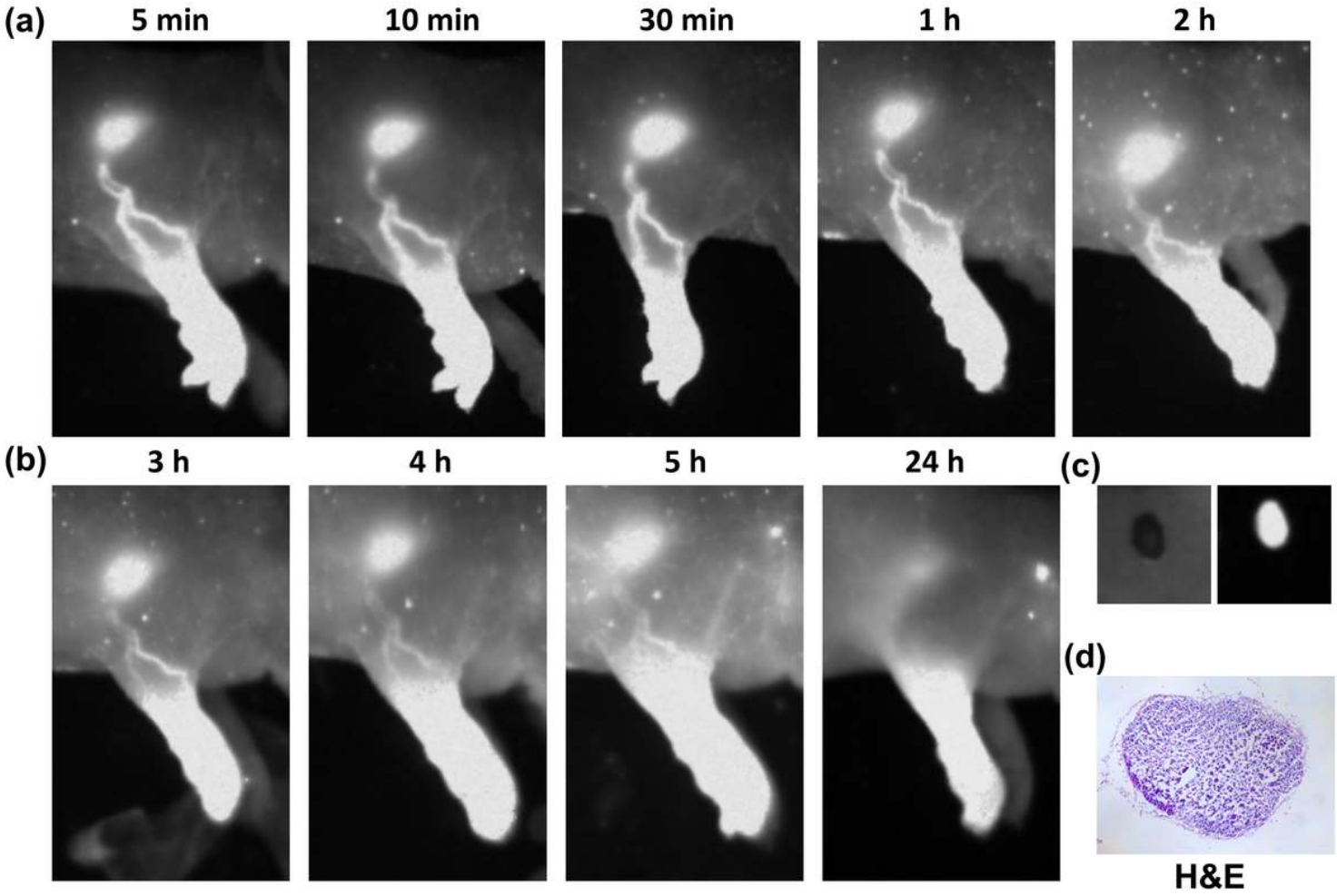

Figure 5

In vivo NIR-II fluorescence imaging of the lymphatic system with PCP-BDP2 NPs. (a b) Fluorescence images of lymph node and lymphatic vessels were captured at 5 min, 10 min, 30 min, 1 h, 2 h, 3 h, 4 h, 5 h, and 24 h respectively. (c) Bright (left) and fluorescent (right) images of sentinel lymph node extracted from the mouse. (d) H&E staining of the excised lymph node.

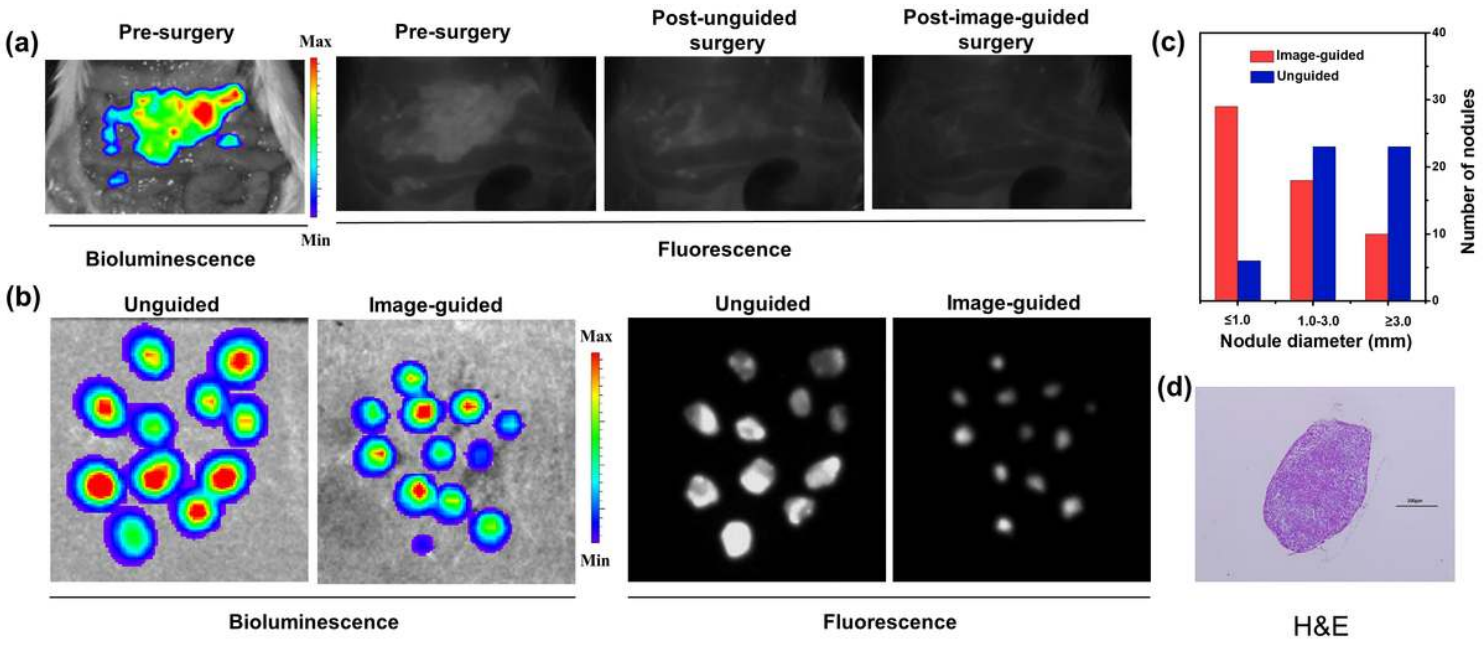

Figure 6

Image-guided surgery of PCP-BDP2 NPs. (a) Bioluminescence and fluorescence imaging of the abdominal cavity before (pre-surgery) and after (post-surgery) tumor resection. (b) Bioluminescence and NIR-II fluorescence signals of the resected nodules of unguided and PCP-BDP2 NPs-guided groups. (c) Statistical chart of nodules diameters resected from fluorescence-guided and unguided groups. (d) H&E staining of excised tumor node.

Supplementary Files

This is a list of supplementary files associated with this preprint. Click to download.

- LKSI20201206.docx
- PCPBDP1.cif
- PCPBDP2.cif
- checkcifPCPBDP1.pdf
- checkcifPCPBDP2.pdf
- 6tilxsuppinfo.docx